

Fuel Regression Modelling for Hybrid Rocket CFD Simulations

*J. E. Durand**, *J. Y. Lestrade***, *J. Anthoine‡*
ONERA/DMPE, Université de Toulouse - F-31055 Toulouse - France

* *jean-etienne.durand@onera.fr*

** *jean-yves.lestrade@onera.fr*

‡ *jerome.anthoine@onera.fr*

†Corresponding author: *jean-etienne.durand@onera.fr*

Abstract

A new Gas-Surface Interaction (GSI) model, based on the mass/energy balance at the fuel surface, is implemented in the ONERA Computational Fluid Dynamics (CFD) software CEDRE. The modelling aims at improving, by means of numerical simulations, the knowledge about aero-thermochemical phenomena in hybrid rocket engines. The two-equation turbulence model $k-\omega$ Shear Stress Transport (SST) is used with wall blowing correction to represent properly the turbulent boundary layer structure which rules the convective transfer and depends on the fuel mass injection. The objective of the study is to validate spatially and temporally the GSI model for H_2O_2 /HDPE HYCAT hybrid rocket engine using a catalytic injector. The validation process is based on the fuel regression rate comparison between numerical CFD results and experimental data from a reference case chosen in the testing campaign of the HYCAT hybrid rocket engine. Particularly, the temporal validation method considers the instantaneous fuel regression rate obtained by a ballistic reconstruction technique from measured instantaneous chamber pressure and oxidizer mass flow rate during the firing test.

1. Introduction

Hybrid rocket engine (HRE) can offer a relevant alternative to solid and liquid propulsion in some space application as apogee mission for geostationary satellites or suborbital transportations for tourism purposes. In fact, the safety is significantly enhanced as propellants are split avoiding hazardous risks and, due to the diffusion-limited phenomenon observed by Marxman,²⁷ thermochemical runaway does not occur contrary to solid propulsion. Furthermore, compared to liquid propulsion, HRE presents higher reliability as the plumb is greatly reduced and no pump is required. About throttability, the hybrid rocket engine is able to stop, start, restart and modulate the thrust by controlling the oxidizer mass flow rate injected in the chamber. About performances, the specific impulse is higher than the values in solid rockets and comparable to the storable/non-cryogenic liquid engines. Beyond these technical advantages, the hybrid rocket is a low-cost propulsion and presents low impact to environment. However, the experimental research though essential is expensive and can hardly give little evidence on the combustion process, controlling the performances of hybrid rocket, wherein the behaviour of the fuel mass flow rate produced by the pyrolysis of the solid fuel plays a key role. Numerical simulations can provide affordable and useful complementary data as the flow represented by the computational results can be easily accessed and handled. However, a useful computed flow field must be able to represent the actual intern ballistic of hybrid rocket engines. Particularly, the fuel regression behaviour has to be modelled with the physical coupling between the fuel regression rate and the thermochemical phenomena in the turbulent boundary layer. The Gas-Surface Interaction model (GSI) enables the simulation to feature the fuel regression rate and the related physical coupling phenomena by considering the conservation of mass and energy exchanges at the fuel surface. Most of authors used this approach for hybrid rocket engine simulations^{4,6,11,21,22,26} to predict propulsive performances and efficiencies or to improve the knowledge of aerodynamics on the fuel regression rate. In the literature, the validation of the numerical modelling is mainly carried out by comparing numerical results with time-space averaged experimental data, particularly for the fuel regression rate. The most usual technique to estimate the time-space averaged fuel regression is to calculate the diameter difference between the initial state and the end of the firing test over the burning time where the final diameter is deduced from the mass loss during the firing test.^{3-6,13,16,17,22,34,35} As the thermal phenomena led by the flow dynamics affect the fuel regression rate, a spatial validation of the GSI model enables the

FUEL REGRESSION MODELLING FOR HYBRID ROCKET CFD SIMULATIONS

modelling to simulate aero-thermal phenomena present in more complex hybrid rocket configurations. Zhang *et al.*,⁴² to highlight the effect of diaphragm on the local fuel regression, compared therefore the fuel regression rate distribution along the port between computations and experimental data by considering diameter variations along the port. Besides, to understand the effects of thermal boundary layer on fuel regression rate, Di Martino *et al.*¹⁴ have compared numerical distribution of fuel regression rate along the fuel and the time averaged local fuel regression rate experimentally obtained by measuring the local final diameter for ABS and HDPE as solid fuels.

However, the internal reactive flow in the fuel port induces temporal variations of the diameter and the fuel regression rate as the fuel degrades during the firing test and the total mass flux through the canal decreases when the port diameter increases. Moreover, the total fuel mass flow rate varies with time as the decrease in fuel regression rate does not compensate generally the fuel surface increase. Because of this oxidizer to fuel ratio shift, the combustion efficiency and propulsive performances are significantly altered. Consequently, a temporal validation of fuel regression model is required to enable the numerical modelling to represent, at a chosen instant, the aero-thermochemical phenomena implying alteration on mixing and performances. Several measurement techniques are able to catch the instantaneous fuel regression rate such as ultrasound measurement method, plasma capacitance gauge method, real time X-Ray Radiography, resistance-based regression measurement technologies, etc. Bianchi *et al.*⁴ were the first to compare numerical simulations of HRE with the experimental space average fuel regression rate with time by means of a ballistic reconstruction technique developed by Carmicino and Russo Sorge.⁹ Bianchi *et al.* have thereby brought evidence for the ability of the spatially averaged fuel regression rate calculated at the averaged port area to represent efficiently the time-averaged value.

The main objective of the present study is to validate spatially and temporally the GSI model implemented in CEDRE software to be able to provide information about the aero-thermochemical flow phenomena occurring in the combustion chamber of a hybrid rocket completing experimental data. The numerical modelling is assessed and the calculation methods of the experimental time averaged fuel regression rate are compared. The instantaneous space averaged fuel regression rate is estimated to show the ability of the GSI model to simulate important instants for research purposes.

2. Experimental available data

2.1 Experimental set-up

To assess the relevance of the numerical models and CFD results, experimental data are required from instrumented lab-scale engine, such as the HYCAT facility (figure 1). The HYCAT facility is made up of four parts: a catalyzer injector, a combustion chamber, a post-chamber and a nozzle. This facility was designed to be able to change the length of each engine part and the fuel grain type.² Even though different propellants can be used, those involved in this paper are HDPE for the fuel and H₂O₂ for the oxidizer.

The engine, which can operate until 7.5 MPa, is instrumented with a Coriolis mass flow meter for the oxidizer and four pressure probes (two just before the combustion chamber and two in the post-chamber) and is connected to a thrust sensor to get the propulsive performances. Temperature and pressure measurements of the liquid oxidizer just upstream of the injector are also included. In order to measure the fuel regression rate instantaneously, the engine is also instrumented with ultrasonic sensors (one located at the head-end of the fuel grain and two at the rear-end).^{10,32} Pulse-echo technique is non intrusive and easy to set up compared to visualization and X-rays measurement techniques.

A catalytic injector, which enables the combustion efficiency to increase relatively to a classical atomizer, is used.²⁴ The catalyzer decomposes the hydrogen peroxide into hot gaseous oxygen and steam water which is then injected through a gaseous injector directly within the combustion chamber without using a pre-chamber. The injection of a hot gaseous oxidizer is expected to improve the mixture with the pyrolysis gas provided by the fuel grain and to avoid losing a part of the generated heat flux to vaporize and warm the liquid oxidizer. The catalytic injector combines a liquid injector plate, a decomposition chamber containing the catalyst particles and a gaseous injector (figure 2). The injector plate was designed in order to spread all the liquid hydrogen peroxide through the cross section of the decomposition chamber. This chamber consists of an Inconel cylinder closed by refractory steel meshes in order to maintain the catalyst particles inside the decomposition chamber. The catalyst, developed and provided by Heraeus, is a Pt based catalyst supported on Al₂O₃ material.²⁵ With the use of catalytic bed, no pyrotechnic device is required to ignite the hybrid engine, improving the safety. The ignition occurs owing to the energy supplied from the hot oxidizer flow. The catalytic bed has therefore to provide a very good efficiency related to a short transient time. A multi-pulsed

operation of the hybrid engine is thereby possible as well. The decomposition temperature is measured at the outlet

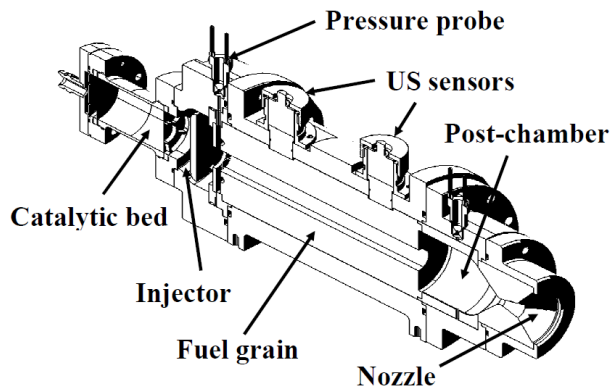


Figure 1: HYCAT facility

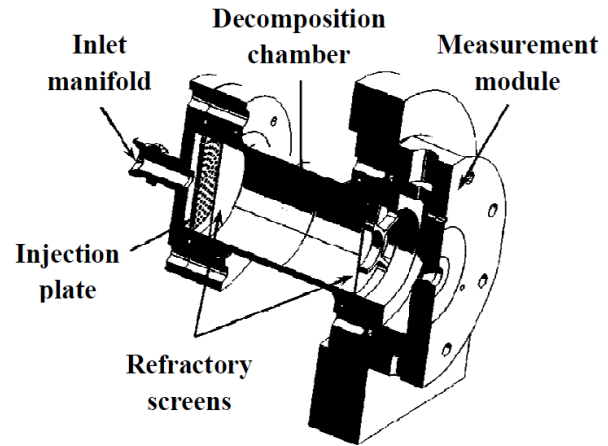


Figure 2: Catalytic injector

of the catalytic bed thanks to three thermocouples. The measurement of the decomposition chamber pressure enables to obtain the characteristic curve (oxidizer mass flow rate as a function of the pressure differential) of this chamber in order to precisely control the operating conditions of the mono-propellant tests and the hybrid firing tests. The synoptic diagram of the measurement chain is indicated in figure 3. According to Lestrade *et al.*,²⁵ the repeatability of the firing tests has been evidenced by comparing two tests performed in the same conditions. The reproducibility error is under 0.6 % for the mean pressure chamber, the characteristic velocity and the mean thrust, except for the oxidizer-to-fuel ratio with 1.8 % of difference.

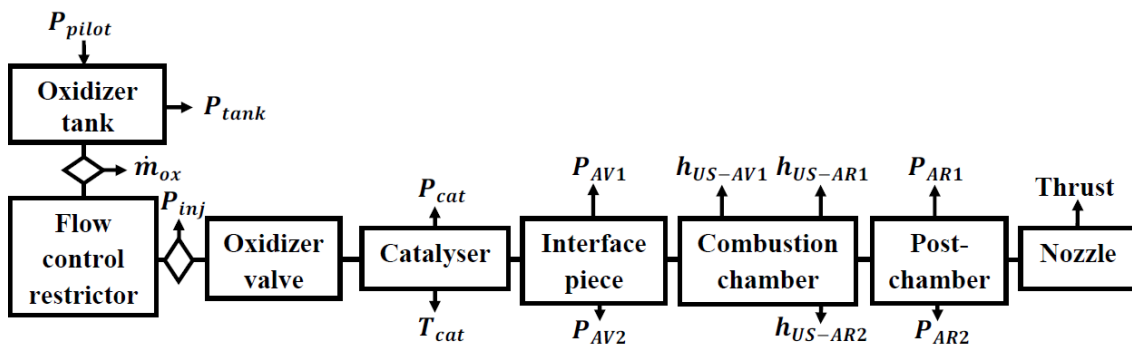


Figure 3: Synoptic diagram of the measurement chain of the HYCAT hybrid engine

Almost all tests of the HYCAT facility used a swirl injection for the oxidizer except for the 12th and the 23th firings where an axial injection was used. HYCAT 12 is chosen as the reference case of simulations with the pyrolysis model described below to limit the size of the computations since 2D axis-symmetric simulations are possible. The fuel grain has a 25 mm diameter single-circular port and a 240 mm length, and the nozzle is conical. The oxidizer is injected axially. Figures 4 provides the temporal evolutions of the combustion chamber pressure P_{ch} , the oxidizer mass flow rate \dot{m}_{ox} , the thrust F_{th} and the oxidizer decomposition temperature T_{cat} for the hybrid test with the axial injector. The averaged characteristics of the reference test are displayed in table 1.

A mono-propellant phase precedes the hybrid mode. When combustion occurs, the diffusion flame increases the chamber temperature and then the characteristic velocity with the effect to provide a higher combustion chamber pressure. This pressure increase reduces the oxidizer mass flow rate compared to its amplitude during the mono-propellant phase. Larger pressure oscillations occurred for axial injector case compared with the swirl injector case in which mixing is enhanced between the hot gaseous oxidizer and the pyrolyzed fuel.² The temperature recorded at the outlet of the decomposition temperature reaches about 875 K, just before the extinction of the engine.

FUEL REGRESSION MODELLING FOR HYBRID ROCKET CFD SIMULATIONS

2.2 Experimental data analysis

The time-averaged fuel mass flow rate \dot{m}_{fuel} is obtained by measuring the mass loss ΔM_{fuel} and the burning time t_b during the firing test:

$$\dot{m}_{fuel} = \frac{\Delta M_{fuel}}{t_b} \quad (1)$$

The burning time is determined by taking the time difference between two peaks of the pressure time-derivative at the beginning and at the end of the hybrid phase. The end-diameter could be determined by measuring the space averaged diameter in the fuel port at the end of the test (D_{end}^{geo}). Nevertheless, another technique is to compute an estimated end test diameter \overline{D}_{end}^{vc} from the mass loss and volumetric conservation by the following expression:

$$\overline{D}_{end}^{vc} = \sqrt{D_{ini}^2 + \frac{4\Delta M_{fuel}}{\pi\rho_f L_{fuel}}} \quad (2)$$

Then, the time averaged fuel regression rate $v_{reg,m}$ and the oxidizer-to-fuel ratio O/F are therefore written as:

$$v_{reg,m} = \frac{\overline{D}_{end} - D_{ini}}{2t_b} \quad \text{and} \quad O/F = \frac{\dot{m}_{ox}t_b}{\Delta M_{fuel}} \quad (3)$$

The test results used for the computation of the time and spatially averaged fuel regression rate are brought together in the table 1. The burning time uncertainty is determined by considering the discrepancies between the before and after the pressure time derivative lobe at the beginning of the combustion process and at the pressure drop zone related to the end of the firing test. The aforementioned uncertainty turns out to be the most determinant for the space averaged fuel regression uncertainty. In fact, the burning time relative uncertainty reaches 5.3 % whereas the uncertainties related to the initial geometry and mass loss are below 0.4 %. By considering the volumetric conservation, the final diameter has an uncertainty equal to 0.3 %.

Table 1: HYCAT 12: reference case

case	HYCAT 12
\dot{m}_{ox} (g.s ⁻¹)	97.7 ± 0.2
D_{ini} (mm)	25.0 ± 0.05
L_{fuel} (mm)	240.0 ± 0.05
d_t (mm)	7 ± 0.05
ΔM_{fuel} (g)	50.0 ± 0.1
t_b (s)	6.3 ± 0.3
P_{ch} (MPa)	3.6 ± 5.0 × 10 ⁻³
O/F	12.4 ± 0.7
η	0.88 ± 0.03
$v_{reg,m}$ (mm.s ⁻¹)	0.40 ± 0.02
\overline{D}_{end}^{vc} (mm)	30.0 ± 0.09
$\overline{D}_{end,m}^{geo}$ (mm)	29.3 ± 0.3

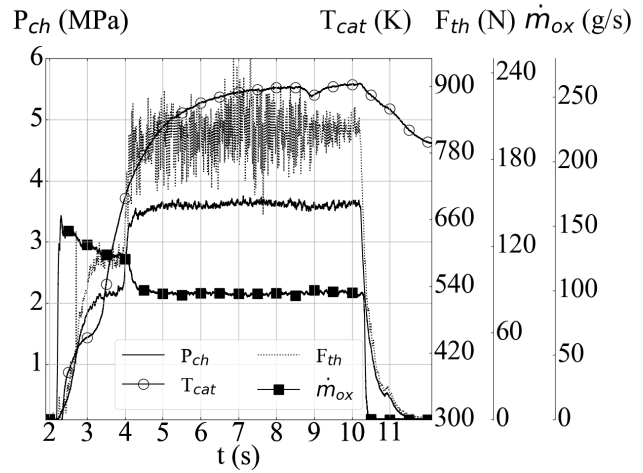


Figure 4: Firing test with catalyzer and the axial gaseous injector

To catch temporal variations of fuel regression rate during a firing test, the ultrasound measurement has been used during the testing campaign. As the sound speed is sensitive to temperature, the fuel regression rate obtained from ultrasound measurement is influenced by the temperature distribution in the fuel. Nevertheless, according to Sorge and Carmicino,³¹ as the HDPE has a very low thermal diffusion value (0.23 mm².s⁻¹), the error in fuel regression rate, is lower than 1.5 %. Unfortunately, the obtained data during the testing campaign cannot be exploited successfully as anomalous trends of the time-to-flight variations with the time have been stated due to thermal effects created by the heat provided by the oxidizer flow to the solid fuel during the mono-propellant phase. A methodology to correct such this phenomenon is currently under development at ONERA to seize conveniently the diameter evolution of the fuel port. In the meantime, alternatively, an estimation of instantaneous space-averaged fuel regression can be obtained from the pressure and oxidizer mass flow rate variations during the hybrid phase. Wernimont and Heister³⁷ built an integral averaged technique for determining the instantaneous regression rate based on the experimental characteristic velocity

FUEL REGRESSION MODELLING FOR HYBRID ROCKET CFD SIMULATIONS

C_{exp}^* which is assumed constant. However, because of the oxidizer-to-fuel ratio shift, that quantity is not strictly constant. Hence, the authors have stated an error of 10% in C_{exp}^* implying a discrepancy of 35 % in instantaneous spatially averaged fuel regression rate. George *et al.*¹⁸ developed a similar approach but considering a constant combustion efficiency. In fact, in a set of repeatable realized tests, the authors found very low variations of combustion efficiency around 1 % and below 2 % for all cases. The discrepancy between measured and computed spatially averaged port diameter at the end of a firing test varied below 2 %. By considering further errors in pressure measurement, temperature and fuel mass flow rate computation, the uncertainty of fuel regression rate is below 3.5 %. Besides, George *et al.* have also assumed that the igniter combustion products do not contribute to the hybrid combustion process. In the present study, a catalytic injector is used avoiding mass flow rate addition due to an igniter. The instantaneous fuel regression rate is therefore estimated by using an improved reconstruction technique from Kumar and Ramakrishna²⁰ which have developed a methodology inspired by George *et al.*

According to the definition of the experimental specific characteristic velocity and the combustion efficiency, the theoretical characteristic velocity can be expressed as:

$$C_{th}^*(O/F) = \frac{P_{ch}A_t}{\eta\dot{m}_{tot}} \quad as \quad \eta = \frac{C_{exp}^*}{C_{th}^*} \quad (4)$$

The total mass flow rate is also written with O/F and the oxidizer mass flow rate:

$$\dot{m}_{tot} = \dot{m}_{ox} \left(1 + \frac{1}{O/F} \right) \quad (5)$$

Hence, an equation system with one equation and one unknown, which is the oxidizer to fuel ratio, is established:

$$g(O/F) = \frac{P_{ch}A_t}{\eta\dot{m}_{ox}} \quad with : \quad g(O/F) = C_{th}^*(O/F) \left(1 + \frac{1}{O/F} \right) \quad (6)$$

The theoretical characteristic velocity is computed by the NASA CEA program in ranges of oxidizer to fuel ratio (0.5 to 30) and pressure (8 to 38 bar). Multiplied by the term $(1 + 1/(O/F))$, the function g turns out to be strictly decreasing. Hence, the given solution is unique.

The total fuel mass flow rate is therefore computed from the oxidizer to fuel ratio:

$$\dot{m}_f = \frac{\dot{m}_{ox}}{O/F} \quad (7)$$

To take into account the lateral burning, the fuel regression rate on the lateral faces is estimated considering the initial solid fuel length and an equivalent length at the end of the firing:

$$v_{lat} = \frac{L_{f,final} - L_{f,ini}}{t_b} \quad (8)$$

As the total fuel mass flow rate is divided between the fuel mass flow rate in the port and the lateral faces, the fuel mass flow rate released in the port is written at the instant $t_n = n\Delta t$:

$$\dot{m}_{f,port,n} = \dot{m}_f - \rho_f v_{lat} \pi \frac{\bar{D}_{ext}^2 - \bar{D}_n^2}{4} \quad (9)$$

Hence, at $t_n = n\Delta t$ the instantaneous fuel regression rate in the port and diameter \bar{D}_n and length L_n of the solid fuel are therefore written as:

$$\bar{v}_{reg,n} = \frac{\dot{m}_{f,port,n}}{\pi \rho_f \bar{D}_n L_{f,n}} \quad and \quad \bar{D}_{n+1} = \bar{D}_n + 2\bar{v}_{reg,n} \Delta t \quad and \quad L_{f,n+1} = L_{f,n} - v_{lat} \Delta t \quad (10)$$

The ballistic reconstruction method has been applied to the 12th test of the HYCAT campaign. The related results are displayed on the table 2 and the temporal evolution of spatially averaged diameter and fuel regression rate in the fuel port are shown in the figure 5. The diameter increases almost linearly with time from $t = 4.3$ s to 10.2 s.

The final diameter is equal to 29.4 mm with a difference of 0.5 % compared to the mean value from measured final diameters and -2 % with the volumetric conservation calculation method. Nevertheless, as lateral faces of the

FUEL REGRESSION MODELLING FOR HYBRID ROCKET CFD SIMULATIONS

Table 2: Comparison between the measured and computed final diameter and length of the solid fuel

	\bar{D}_{end} (mm)	ΔM_{fuel} (g)
Measured data	29.3 ± 0.3	50.0 ± 0.1
Reconstruction technique	29.4	49.8
ϵ (%)	0.5	0.5

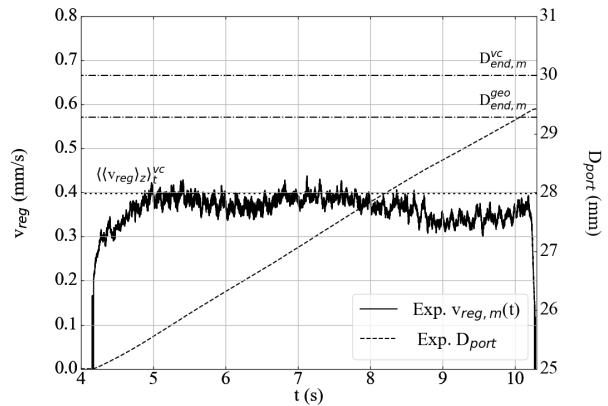


Figure 5: Instantaneous spatially averaged fuel regression rate and diameter evolution during the HYCAT 12 firing test

solid fuel undergo pyrolysis as well, the lateral mass loss is not removed from the total mass loss for considering a diameter calculation with a constant solid fuel length. Hence, with the aforementioned method, the obtained diameter naturally overestimates the actual one. The spatially averaged fuel regression rate shows a stable intensity level during the hybrid phase. Nevertheless, despite a noisy evolution, the global trend oscillates slightly with a period coarsely equal to the half of the burning time.

3. Numerical models

The simulations are made with CEDRE, the ONERA's CFD software which is a multi-physics platform on general unstructured grids, for both research and industrial applications, in the fields of energetics and propulsion.³⁰ The software architecture follows a multi-domain, multi-solver approach. Solvers are considered for each physical system: gas phase (CHARME), dispersed phase (SPARTE), thermal fields in solids (ACACIA) and radiation (REA and ASTRE). These solvers share the CEDRE architecture and libraries, and can be coupled to perform a multi-physics computation or be operated alone. As only reacting multi-species gaseous flow is considered, the solver CHARME is therefore enough in this study. A numerical study has been initiated by Durand *et al.*¹⁵ to improve the knowledge about the impact of thermal radiation on fuel regression rate by coupling the CHARME solver with ASTRE solver which computes the radiative transfer by a particular application of the Monte Carlo Method.

Following the classical approach of hybrid rocket computations, a quasi-steady flow is assumed as, according to Sankaran,³³ the fuel regression rate, typically about $0.1\text{-}0.5\text{ mm}\cdot\text{s}^{-1}$, is extremely small compared to the longitudinal velocity in the port, about $25\text{-}70\text{ m}\cdot\text{s}^{-1}$, for $G_{ox} = 200\text{ kg}\cdot\text{m}^{-2}\cdot\text{s}^{-1}$ at the port inlet. Hence, the density based approach is applied to get a steady solution from an unsteady computation by introducing a numerical time step.

The simulated reference case, HYCAT 12, presents an axial injection and the problem could be reduced to a 2D axis-symmetric field. Hence, the flow is assumed 2D axis-symmetric for the HYCAT configuration simulated here and the test case as well. As the liquid hydrogen peroxide is catalysed into steam water and gaseous oxygen in the inlet and the solid fuel HDPE is assumed to decompose chemically into gaseous ethylene, only gaseous multi-species phase is considered containing five species: C_2H_4 , O_2 , H_2O , CO and CO_2 . Other hydrocarbon species can be added to compute the multi-species pyrolysis. In this paper, ethylene is assumed to be the only product of pyrolysis. A future study will provide a more comprehensive pyrolysis model by taking into account several pyrolysis products. The heat capacity is computed as a 8th order's polynomial function in temperature. The dynamic viscosity is expressed by the Sutherland's law and the thermal conductivity formulation is based on the Eucken's approach. The species diffusivity is obtained from a constant laminar Schmidt number equal to one based on the the phase kinematic viscosity calculated from the local species mixing. The flow is assumed compressible to consider density variation in reacting flow and to be able to compute in the nozzle field correctly.

As the Reynolds number in the port is about 10^5 , the boundary layer is assumed turbulent. The flow is therefore computed from the Compressible Reynolds Averaged Navier-Stokes equations.⁴⁰ The turbulent closure model used for

computation is the two-equation eddy-viscosity model $k-\omega$ Shear Stress Transport (SST), developed by Menter *et al.*,²⁸ which combines the advantages of $k-\epsilon$ model in the flow and the advantages of $k-\omega$ model close to the walls by using a blending function and therefore is adapted for internal flow. Particularly, Low Reynolds Number correction is used.⁴¹ The turbulent heat flux is described by using the Reynolds analogy and assuming a constant turbulent Prandtl number equal to 0.9. The same is assumed to the turbulent mass diffusion flux with a constant turbulent Schmidt number equal to 0.9.

As the flow is assumed in chemical non-equilibrium, finite rate kinetic reaction model is used. Two-step reaction system is taken into account for the combustion of ethylene, according to Westbrook and Dryer³⁸ to reduce the computation cost. As non-premixed flame is resolved, thermal and mass turbulent diffusions mainly rule the combustion process in which the accuracy of the chemical kinetic mechanism may therefore play a minor role where the Damköhler number is very high (fast chemistry). The fuel surface where pyrolysis phenomenon occurs is considered by introducing a gas-surface interaction model which is based on the mass and energy balances.

The Riemann problem is resolved approximately by the standard version of Harten-Lax-van Leer-Contact solver, developed by Toro *et al.*,³⁶ which is quite robust and efficient, to reduce the computation cost.

3.1 Gas-surface interaction (GSI) model

As pyrolysis phenomenon is a chemical degradation of the solid fuel, the fuel mass flow rate introduced in the flow is therefore related by the mass conservation and the energy exchange on the surface between the gas-phase flow and the solid fuel. Hence, according to the mass conservation, fuel mass flow rate can be written as:

$$G_f = (\rho v)_w = \rho_s v_{reg} \quad (11)$$

where G_f is the fuel mass flux ($\text{kg}\cdot\text{m}^{-2}\cdot\text{s}^{-1}$), ρ and v are respectively the density and the velocity of the injected gas-phase flow due to fuel regression, and ρ_s and v_{reg} are respectively the solid fuel density and the fuel regression rate. During the pyrolysis process, the pyrolyzed species are carried in the flow by mass diffusion and mass transport from the fuel surface. The production rate of the i^{th} species $\dot{\omega}_i$ by pyrolysis is the source term in the mass flux balance at the fuel surface. Hence, mass flux balance for each species are written as:

$$\forall i \in [1, N_{esp}], \quad y_i G_f - \rho D_{m,i} \left. \frac{\partial y_i}{\partial \eta} \right|_{w+} = \dot{\omega}_i \quad (12)$$

where $D_{m,i}$ is the mass diffusivity of the species i to the gas mixing. To respect the global mass conservation, the sum of the all source terms is equal to the total fuel mass flux released in the flow:

$$\sum_{i=1}^{N_{esp}} \dot{\omega}_i = G_f \quad (13)$$

The energy exchange balance can be written as:

$$\lambda_g \left. \frac{\partial T}{\partial \eta} \right|_{w+} + \Phi_{rad}^{net} - \sum_{i=1}^{N_{esp}} \dot{\omega}_i h_{i,w} = -G_f h_s + \lambda_s \left. \frac{\partial T}{\partial \eta} \right|_{w-} \quad (14)$$

where, T is the temperature, $w+$ and $w-$ are the wall neighbours respectively in the flow and in the solid fuel. $h_{i,w}$ and h_s are, respectively, the enthalpies of the i^{th} species and the solid fuel at the wall. $D_{m,i}$ is the mass diffusivity coefficient of interaction between the mixture and the i^{th} species, λ_g and λ_s are the conductivity respectively in the gas and in the solid fuel, and Φ_{rad}^{net} is the net heat flux provided by thermal radiation. The radiative contribution is neglected as the oxidizer mass flux crossing through the port is about $200 \text{ kg}\cdot\text{m}^{-2}\cdot\text{s}^{-1}$ which is high enough (Chiaverini *et al.*¹²) to enable the thermal convection to prevail at the wall. As the flow is assumed steady, the gas-solid interaction model is also written in steady regime. Hence, using the quasi-steady heat equation in solid phase with bulk motion, the temperature gradient at wall in the solid fuel can be expressed by:

$$\lambda_s \left. \frac{\partial T}{\partial \eta} \right|_{w-} = G_f C p_s (T_w - T_0) \quad (15)$$

where $C p_s$ is the mass heat capacity of the solid fuel, T_w and T_0 are the temperature respectively of the wall and deep below the wall. Species and solid enthalpies (resp. $h_{g,w}$ and h_s) can be written by the following expressions:

$$h_{g,w} = \sum_{i=1}^{N_{esp}} y_{i,w} \left[\int_{T_0}^{T_w} C p_{m,i}(T) dT + \Delta H_{f,i}^\circ \right] \quad \text{and} \quad h_s = C p_s (T_w - T_0) + \Delta H_{f,s}^\circ \quad (16)$$

FUEL REGRESSION MODELLING FOR HYBRID ROCKET CFD SIMULATIONS

As the wall species distribution is calculated by the model, the aforementioned condition is imposed in the stoichiometric coefficients. According to the reaction extent table, the source terms are computed from the extent of reaction related to the total fuel mass flux. Thus, by considering a solid fuel C decomposing thermally in N_p products:

$$C \Rightarrow \sum_{k=1}^{N_p} \nu_k P_k \quad (17)$$

where ν_k is the stoichiometric coefficient of the k^{th} pyrolysis product. The source terms related to the pyrolysis products are written as:

$$\forall k \in \llbracket 1, N_p \rrbracket, \quad \dot{\omega}_{pyr,k} = \frac{\nu_k M_{P_k} G_f}{M_C} \quad \text{and} \quad M_C = \sum_{k=1}^{N_p} \nu_k M_{P_k} \quad (18)$$

In the study, no surface reaction is considered as oxidation and hydrolysis have little effect on HDPE. Hence, for species coming from the gaseous flow, such as molecular oxygen and steam water, and not produced by pyrolysis have a source term equal to zero. The summation condition of source terms is thereby respected.

$$\sum_{i=1}^{N_{exp}} \dot{\omega}_i = \sum_{k=1}^{N_p} \dot{\omega}_{pyr,k} = \sum_{k=1}^{N_p} \frac{\nu_k M_{P_k} G_f}{M_C} = G_f \quad (19)$$

Using all assumptions established previously, the energy exchange balance can be expressed in neglecting radiative contributions:

$$\lambda_g \left. \frac{\partial T}{\partial \eta} \right|_{w+} = \sum_{k=1}^{N_p} \dot{\omega}_{pyr,k} h_{k,w} - G_f \Delta H_{f,s}^{\circ} \quad (20)$$

The pyrolysis of the solid fuel HDPE is assumed to produce only one species: gaseous ethylene. Hence, the production rate of ethylene is equal to the total fuel mass flux G_f and, for the other species, the production rate is equal to zero.

The production rate of ethylene, produced by pyrolysis, is described by an Arrhenius law:

$$G_f = \dot{\omega}_{pyr,C_2H_4} = A e^{-\frac{E_a}{RT_w}} \quad (21)$$

where A is the pre-exponential coefficient in $\text{kg.m}^{-2}.\text{s}^{-1}$ and E_a the activation energy in kJ.mol^{-1} . The value of these coefficients are reported in the table 3 found by Lengellé *et al.*²³ Concurring with Bianchi *et al.*,⁶ significant discrepancies of the pyrolysis enthalpy ΔH_p of HDPE have been found in the scarce available literature. Lengellé *et al.*²³ have given a value of such pyrolysis enthalpy equal to $-2.72 \times 10^6 \text{ J.kg}^{-1}$. However, because of the lack of new measurement, Bianchi *et al.*⁶ have arbitrarily reduced the reported value by 30 %. For these reasons, as the present paper aims at reproducing with the least error possible in data and the existing value of pyrolysis enthalpy may take into account other species than ethylene, the standard formation enthalpy of HDPE used in HYCAT campaign is measured by the calorimetric bomb, reported on the table 3.

Table 3: Thermochemical data for pyrolysis of HDPE

	Lengellé <i>et al.</i> ²³		ONERA new measurement 2018
	$A_{pre} (\text{s}^{-1})$	$E_a (\text{J.mole}^{-1})$	$\Delta H_{f,HDPE}^{\circ} (\text{J.kg}^{-1})$
HDPE	2×10^{16}	2.512×10^5	$-6.4 \times 10^5 \pm 1 \times 10^4 (20 : 1)$

3.2 GSI model numerical resolution method

The resolution of the GSI model is performed, by considering the vector \mathbf{U} bringing together the wall temperature, the normal velocity to the wall and species mass fractions, from the Newton method applied to residuals of conservation equations featured by the vector \mathbf{R} which must tend to 0 vector to respect the conservation of all integrated quantities as energy exchange, species masses and total mass.

$$\mathbf{U} = \begin{pmatrix} T \\ V_n \\ y_1 \\ \vdots \\ y_{N_{exp}} \end{pmatrix} \quad \text{et} \quad \mathbf{R} = \begin{pmatrix} -\rho D_{m,1} \frac{(y_{1,i} - y_{1,w})}{\delta x} + y_{1,w} G_f(T_w) - \dot{\omega}_1(T_w) \\ \vdots \\ -\rho D_{m,N_{exp}} \frac{(y_{N_{exp},i} - y_{N_{exp},w})}{\delta x} + y_{N_{exp},w} G_f(T_w) - \dot{\omega}_{N_{exp}}(T_w) \\ G_f(T_w) \left[\sum_{k=1}^{N_{pyr}} \frac{\nu_k M_{P_k}}{M_C} h_{P_k,w} - \Delta H_{f,s}^{\circ} \right] - \lambda_g \frac{(T_i - T_w)}{\delta x} \\ V_n - \frac{G_f(T_w)}{\rho} \end{pmatrix} \quad (22)$$

where $V_n = \vec{V} \cdot \vec{n}$. The jacobian matrix is obtained by the perturbation method.

3.3 Turbulence-surface mass injection interaction correction for k- ω SST

The fuel regression rate intensity depends on the heat flux at the wall given mainly by the thermal convection which is characterized by the temperature profile in the turbulent boundary layer structure altered by roughness or surface mass injection. However, the k- ω turbulence models for CFD simulations are designed for smooth, non permeable walls and require therefore a modification to take into account the impact of injected fluids. Wilcox³⁹ has proposed a correction of the specific dissipation rate at wall which is possible as ω -oriented equations possess solutions in which the value of ω can be specified arbitrarily at the wall. The correction is based on the measurement of velocity profile in a turbulent boundary layer with surface mass injection realized by Andersen *et al.*¹ The value of the turbulent kinetic energy is equal to zero and the specific dissipation rate depends therefore on the parameter v_w^+ the reduced normal velocity at the wall:

$$v_w^+ = \frac{v_w}{u_\tau} \quad (23)$$

where v_w is the normal velocity at the wall and u_τ the shear velocity. The value of ω at the surface is expressed with a correction number S_B :

$$\omega = \frac{u_\tau^2}{\nu} S_B \text{ at } y = 0 \quad (24)$$

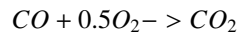
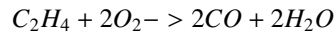
The value of S_B has been modified until an optimum matching with the measured velocity profile obtained by Andersen *et al.*¹ providing the final correction S_B expressed by:

$$S_B = \frac{20}{v_w^+ (1 + 5v_w^+)} \quad (25)$$

Recently, using the correction proposed by Wilcox,³⁹ Hink¹⁹ has validated the k- ω SST turbulence model in the thermal boundary layer of effusive cooled walls for material protection in aerospace combustion chamber. The research work of Hink is very important for hybrid rocket computation as this turbulence model is validated, not only for the velocity profile in the turbulent boundary layer but also for the temperature profile and the heat flux at the wall. Experimental data are provided by Moffat *et al.*²⁹ and performed on porous flat plate to determine the velocity and temperature profiles for which the measurements have shown an error below 1 %.

3.4 Gas reaction model

The actual reaction is very complex involving high quantity of radical-type species in very numerous reaction steps. The hybrid rocket CFD requires therefore reduced mechanisms to reduce the computation cost. The global mechanism proposed by Westbrook and Dryer³⁸ for the combustion of ethylene is therefore chosen for the current computation. The finite rate reactions are modelled by two reaction steps:



The rate of consumption for each species are written as:

$$\dot{\omega}_{C_2H_4} = -M_{C_2H_4} k_{f,1} [C_2H_4]^{0.1} [O_2]^{1.65}$$

$$\dot{\omega}_{O_2} = -M_{O_2} \left(2k_{f,1} [C_2H_4]^{0.1} [O_2]^{1.65} + 0.5 \left(k_{f,2} [CO] [O_2]^{0.25} [H_2O]^{0.5} - k_{b,2} [CO_2] \right) \right)$$

$$\dot{\omega}_{CO} = M_{CO} \left(2k_{f,1} [C_2H_4]^{0.1} [O_2]^{1.65} - \left(k_{f,2} [CO] [O_2]^{0.25} [H_2O]^{0.5} - k_{b,2} [CO_2] \right) \right)$$

$$\dot{\omega}_{H_2O} = 2M_{H_2O} = 2k_{f,1} [C_2H_4]^{0.1} [O_2]^{1.65}$$

$$\dot{\omega}_{CO_2} = M_{CO_2} \left(k_{f,2} [CO] [O_2]^{0.25} [H_2O]^{0.5} - k_{b,2} [CO_2] \right)$$

The forward and backward reaction rates, k_f and k_b , for the two reactions are expressed as Arrhenius functions in the form $k = AT^n e^{-T_a/T}$, and the values of the constants used in this study are in the table 4.

FUEL REGRESSION MODELLING FOR HYBRID ROCKET CFD SIMULATIONS

Table 4: Arrhenius coefficients for chemical reaction kinetic mechanism³⁸

	A	n	T_a (K)
$k_{f,1}$	7.589×10^7	0.0	15097.2
$k_{f,2}$	1.259×10^{10}	0.0	20130.3
$k_{b,2}$	5.000×10^8	0.0	20130.3

3.5 Numerical method

The HYCAT rocket engine configuration is studied numerically for comparison with experimental data (figure 6). The oxidizer flux, inflowing a gaseous mixing of steam water and dioxygen due to the catalytic decomposition of hydrogen peroxide H_2O_2 at 87.5 %, is set at 876 K at the inlet and the mass flow rate is 97.7 g.s^{-1} . As the turbulent intensity set at the inlet has almost no impact in the injection zone, the level is arbitrarily chosen 10 % at the exit of the catalyzer. The post-chamber wall and injector wall are assumed adiabatic.

All considered meshes, designed with GMSH software, are two dimensional as the inlet flow is injected axially. The choice of structured meshes is taken because the quantity of cells is lower than in unstructured meshes, the regularity of cells is better controlled as the GSI model is sensitive to the mesh quality (figures 6).

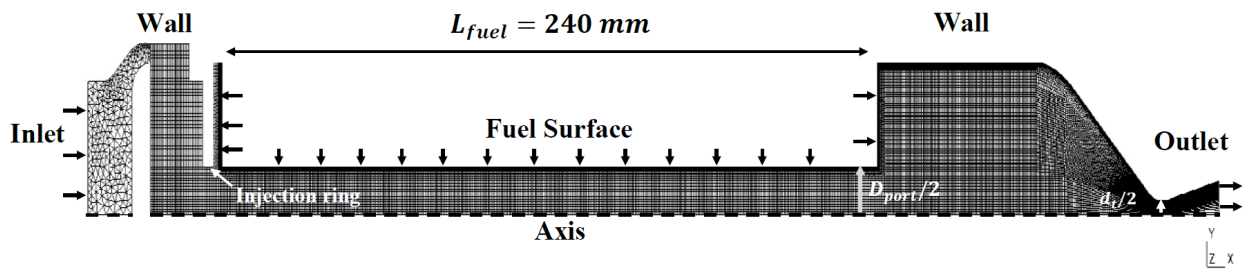


Figure 6: Mesh of the HYCAT configuration

Over the solid fuel boundary, $y^+ = 1$ is obtained for a cell transversal length equal to $5 \mu m$. Hence, the mesh is carefully refined over the fuel surface (figure 7). As the cavity in the inlet region enables to delete the turbulence effects initiated at the inlet boundary before the oxidant's inflowing through the injector ring, unstructured meshing approach is used in the inlet region. The mesh nozzle region is poorly meshed intentionally as the nozzle has to provide only choked conditions in the chamber (figure 8).

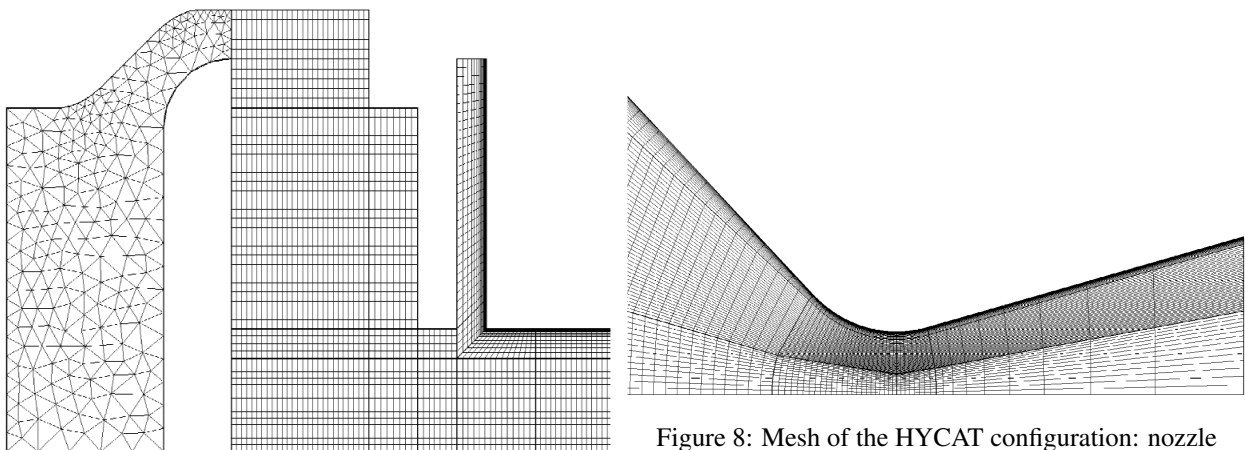


Figure 8: Mesh of the HYCAT configuration: nozzle

Figure 7: Mesh of the HYCAT configuration: injection zone

FUEL REGRESSION MODELLING FOR HYBRID ROCKET CFD SIMULATIONS

The spatial discretization is second-order accurate. The temporal integration is based on Euler's implicit method with a fixed time step of 10^{-6} s (without local time stepping). However, a time step of 10^{-7} s is applied at the beginning of the computation because of the flow perturbation caused by the oxidizer injection and the outflow through the non choked nozzle. The iterative convergence is based on the generalized minimal residual method (GMRES) with 20 internal iterations and a 10 % relative difference as criterion.

Two approaches is used in this study to assess the mesh convergence. Firstly, integral values are considered as the averaged fuel mass flow rate and the chamber pressure. Secondly, global discretization estimation is performed according to the method described by Bonfiglioli and Paciorri.⁷ With the aforementioned approach, the order of accuracy of the scheme and the global grid convergence ratio are estimated, providing further information to the discretization error value.

The convergence of the computations is assumed when mean pressure variations are under 1 %. Grid convergence is based on multiple refined spatial grid computations by a factor 2. The mesh convergence is reached with about 790000 elements (Table 5). Only the pressure level is considered to check the order accuracy of the spatial discretization scheme of the solutions. The figure 9 shows that the global order, $n = 1.91$, is very close to the second order of the spatial discretized scheme used in the computations. Hence, the numerical solution is in the asymptotic convergence range with a grid convergence ratio equal to 0.27. The discretization error is estimated, based on bar unity, around -3.6 which means a difference less than 0.8 % in pressure.

Table 5: Mesh convergence for HYCAT configuration

N° of cells	P (MPa)	\dot{m}_f (g.s ⁻¹)
2.1×10^5	3.75	9.35
7.9×10^5	3.497	8.36
3.2×10^6	3.473	8.46

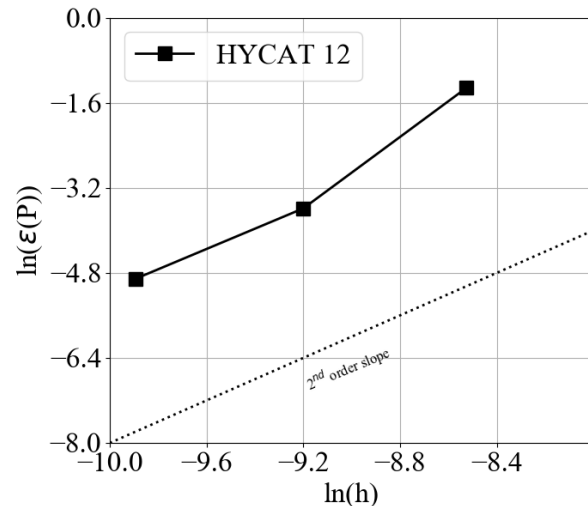


Figure 9: Discretization error of pressure for the HYCAT configuration

4. Results and discussion

The spatially and temporally validation of the presented numerical modelling is organized in two main steps:

- The spatial validation is firstly carried out by comparing the computed fuel regression rates between the initial and final cases of the HYCAT configuration to the experimental time-averaged fuel regression rate varying along the port from diameter measurement after the firing test.
- Secondly, the temporal validation consists in comparing the spatial average computed fuel regression rate to the experimental one at particular instants chosen regularly during the burning phase. Each instant are related to the instantaneous spatially averaged diameter, fuel length and fuel regression rate provided by the ballistic reconstruction technique previously presented. Hence, for each instant, a numerical computation of the HYCAT configuration is carried out with a port diameter and a fuel length set at the values related to the aforementioned instant to compare the spatially averaged fuel regression obtained by the computation with the related experimental fuel regression rate.

FUEL REGRESSION MODELLING FOR HYBRID ROCKET CFD SIMULATIONS

The results are analysed to assess the proposed modelling to compute efficiently the most representative flow of the actual HRE ballistic.

4.1 Experimental temporal averaged assessment of GSI model

To estimate the numerical time averaged fuel regression rate in HYCAT 12 configuration, two computations are carried out based on the initial port diameter and the end port diameter. However, at the end of the firing test, the fuel surface is not uniform which implies variations of section diameter and deformations along the port. Even though a diameter profile along the port for computation can be imposed according to the shape left by the burning after the firing test, a simpler approach is to use a constant equivalent final diameter. Nevertheless, several methods are used in which the most common is based on the volumetric conservation where the mass loss is taken into account. Besides, spatial average of diameter is another possibility which needs to be tested.

The experimental time averaged fuel regression rate is based on the local diameter difference between the initial and the final hybrid phase steps (equation (26)). After the firing test, the burnt solid fuel is sliced perpendicularly to the axis and regularly in eight parts with a thickness of 3 cm. Because, for a given section in the port, the shape is not actually circular, an angular average diameter is obtained, providing the uncertainty as well. The measurement is carried out by using micrometers in range 25-30 mm and 30-40 mm.

$$\langle v_{reg} \rangle_t(z) = \frac{D_{end}(z) - D_{ini}}{2t_b} \quad (26)$$

The final diameter profile along the fuel port is shown with the related uncertainty in the figure 10. The first displayed diameter, equal to 23.3 mm is surprisingly lower than the initial diameter (25 mm) as fuel degradation is expected. Whereas, the other measurement points have more coherent values with a minimum at 28.83 mm, superior to the initial diameter. In fact, a bulge due to the HDPE melt is formed at the inlet (figure 11). The formation of such a bulge might come from the fact that the HDPE at the top surface of the solid fuel is heated by the flow but not enough to lead to pyrolysis. Thus, the flow drags from the top lateral face of the solid fuel to the inlet the melted HDPE until the pyrolysis process starts. Permanently fed in melted HDPE, the inlet section remains therefore with a diameter close or superior to initial one.

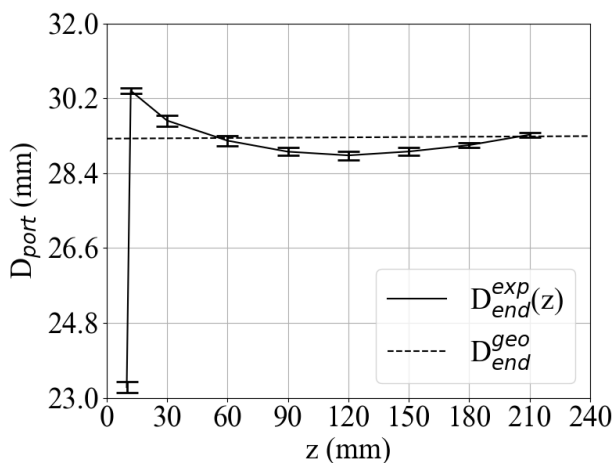


Figure 10: Final diameter variations along the port

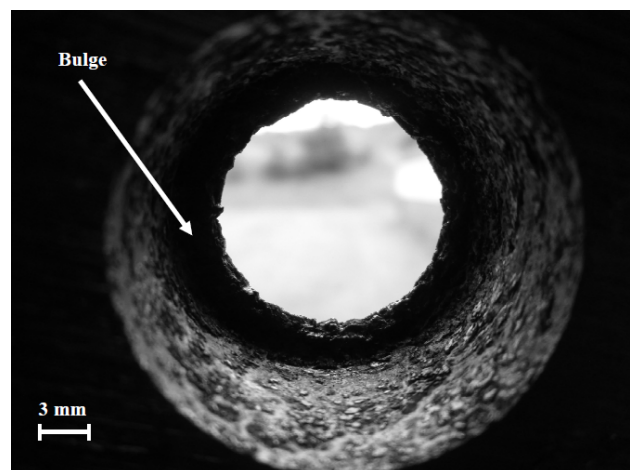


Figure 11: Bulge at the fuel port inlet due to the melted HDPE

Downstream the bulge, the port shape draws a convex parabolic curve with a minimum diameter value equal to 28.83 mm at $z = 120$ mm. The axis averaged final diameter is almost equal to the diameter at $z = 210$ mm and shows that the two first measured points at $z = 12$ mm and $z = 30$ mm cause a higher mean value. The time averaged fuel regression rate along the port is therefore minimal at $z = 120$ mm whereas, close to the ends of the port, the fuel regression rate is more important as seen in the figure 12. Classically, the decrease in fuel regression along the first part of port is due to less stiff boundary layer temperature and velocity gradients at the fuel surface as the turbulent boundary layer increases in the downstream direction. However, from $z = 120$ mm, the fuel regression rate start increasing because of

FUEL REGRESSION MODELLING FOR HYBRID ROCKET CFD SIMULATIONS

the total mass flux increase along the port as the fuel degradation is mainly due to the thermal convection. Hence, the studied case is coherent with the aforementioned explanation.

In the present study, the spatial average of final diameter is used in calculation. This approach is then compared with the case with an irregular port shape built with a piecewise linear function set by the diameter measurements.

In the figure 12, the numerical results using a constant spatially averaged final diameter are compared with the experimental data. The discrepancies in fuel regression rate are below 20. %. Particularly, at $z = 30$ mm and $z = 60$ mm, the discrepancies are below the uncertainty (≤ 4 %) whereas, at $z = 150$ mm and $z = 180$ mm, the numerical fuel regression rate is about 14 % higher than the experimental value. The numerical fuel regression rate overestimates fairly the experimental one from $z = 90$ mm to exit of the port whereas, close to the port inlet, the experimental fuel regression rate is higher than the numerical value and, furthermore, with contradictory trends. Closer to the port inlet, the numerical fuel regression drops contrary to the experimental value which goes on increasing. These observations lead to the fact that the numerical fuel regression profile along the port does not follow the experimental trend due to the shape of the fuel port which alters the aero-thermochemical flow and, consequently, the wall heat flux. Particularly, at the port inlet, the experimental fuel regression rate at $z = 12$ mm is notably high compared with the other measurements. In fact, just downstream the inlet, the formed bulge creates a step flow where the recirculation zone enhances the wall heat flux and, consequently, the fuel regression rate. In contrast, in numerical cases, because of the modelling, the solid fuel cannot be altered by the flow. Hence, as the diameter remains constant along the port, no step flow is observed and the injected flow is readjusted upstream by the cavity left between the injector and the fuel. The fuel regression rate increases therefore strongly at the inlet zone until the neighbourhood of $z = 30$ mm from which the trends of fuel regression rate become stable until the exit of the port.

To improve the comparison, a HYCAT 12 configuration with irregular variations of port diameter shaped by the diameter measurements obtained after the firing test is simulated. The results, shown in the figure 13, seem to follow the experimental fuel regression rate trends even though the differences strongly increase about 20 % at $z = 60$ mm and $z = 90$ mm whereas the numerical value in the constant diameter case is below the uncertainty. The comparison is improved at $z = 12$ mm where the fuel regression rate discrepancy is 15.3 %, and at $z = 150$ mm and $z = 180$ mm with 5.2 % and 0.7 % of differences. Hence, the computed fuel regression rate fits better in the regions where the previous comparison failed even though the calculated fuel regression profile is very unstable. Nevertheless, to damp the obtained distribution, the shape must be improved by considering other measurements or higher interpolation order.

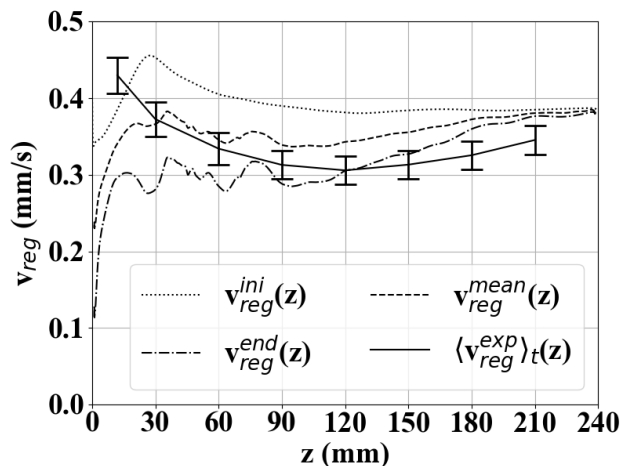


Figure 12: Time averaged fuel regression rate along the port for constant end port diameter calculation

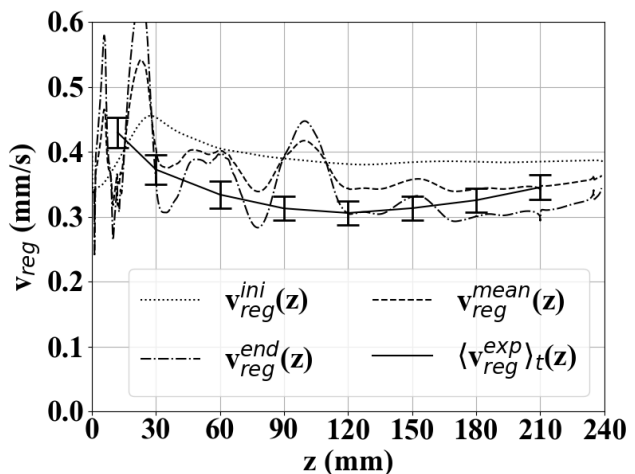


Figure 13: Time averaged fuel regression rate along the port for irregular end port diameter shape calculation

Despite the spatial distribution of the time averaged fuel regression rate is not validated, the spatial-time averaged fuel regression rate is lower than 10 % for the constant diameter cases and 13.3 % for the irregular shaped fuel port. Using the constant diameter assumption, the numerical modelling is assessed by comparing through instants of the hybrid phase, the instantaneous spatial averaged fuel regression rate between computations and experimental time

FUEL REGRESSION MODELLING FOR HYBRID ROCKET CFD SIMULATIONS

dependent results provided by the ballistic reconstruction technique.

4.2 Experimental instantaneous space averaged assessment of GSI model

In this study, an attempt to validate temporally the proposed numerical modelling is presented. The ballistic reconstruction technique is used to get the instantaneous spatially averaged fuel regression rate during the hybrid phase.

Before assessing the numerical modelling for CFD simulation, a short sensibility study is carried out to show the impact of the burning time deviation on fuel regression rate value. In fact, the uncertainty related to the burning time is difficult to establish as no information, at the shutting down of the oxidizer valve, is provided about the fuel pyrolysis and the residual consumption of HDPE which could alter significantly the mass loss estimation during the burning phase. Here, the burning time uncertainty is estimated by considering the lobe thickness of peaks of time derivative of pressure. Nevertheless, using other proposed estimation methods (Carmicino *et al.*⁸), the uncertainty value would be much higher.

The figure 14 shows respectively the maximal errors in diameter and fuel regression with the time during the hybrid phase when the burning time is overestimated according to the uncertainty value calculated in this study: ± 0.3 s, *i.e.* 5.3 % of the estimated burning time equal to 6.3 s. Thus, for a shift of 4.8 % of the burning time value, the diameter discrepancy remains lower than 1.2 % whereas, from $t = 4.5$ s to the end of the firing test, the difference is located between 7 % and 8 %. Hence, the spatial averaged fuel regression rate uncertainty is higher than the one related to the burning time of which uncertainty estimation is therefore critical for the reconstruction of the instantaneous spatially averaged fuel regression rate accuracy.

From HYCAT 12 instantaneous data, the ballistic reconstruction method reproduces the temporal evolution of spatially averaged diameter and fuel regression rate in the fuel port (figure 15). The instantaneous experimental thereby obtained is used for comparison with numerical simulations. As the numerical modelling is established for steady regime and, according to Sankaran,³³ the characteristic time of fuel regression is much higher than the one related to the flow, several steady computations are performed for each chosen instant during the hybrid phase. From ignition at $t = 4.3$ to 10.2 s, the instants 5.5, 7.5, 9.5 s are chosen showing a regular probing during the hybrid phase. By the ballistic reconstruction technique, the spatially averaged diameter and fuel regression rate associated to each instant are obtained and displayed in the table 6.

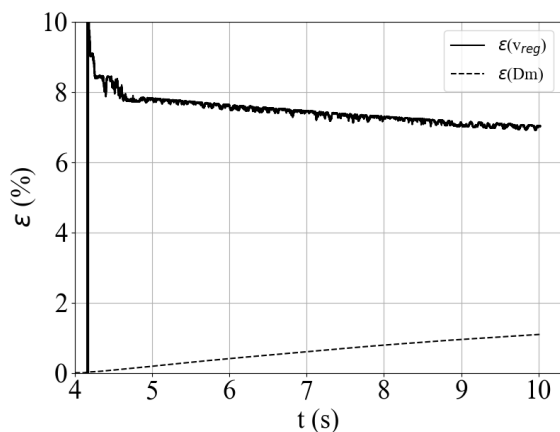


Figure 14: Instantaneous fuel regression rate and diameter deviation evolution for $t_b = 6.3 \pm 0.3$ s

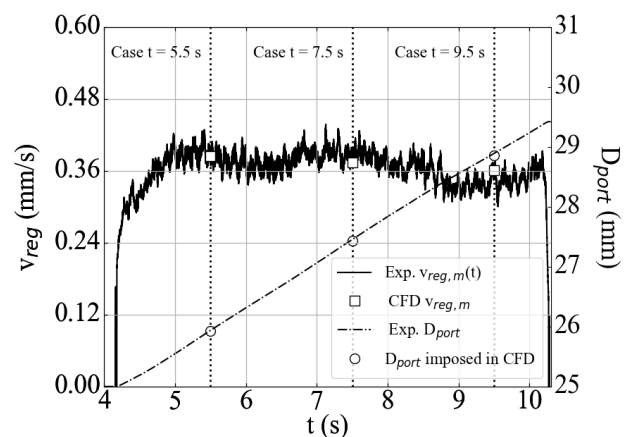


Figure 15: Instantaneous fuel regression rate during the HYCAT 12 firing test and chosen comparison instants

For each instant, the numerical simulation is carried out considering a constant port diameter and a fuel length set at the values obtained by the Reconstruction method corresponding to that instant. The mean computed fuel regression is obtained by averaging spatially the fuel regression only along the fuel surface. To compare reliably with numerical data, because of the strong observed noise, the instantaneous fuel regression rate is averaged over an temporal interval around the chosen instant¹⁵ with a length equal to 0.1 s. The results of fuel regression rate comparison is presented in

FUEL REGRESSION MODELLING FOR HYBRID ROCKET CFD SIMULATIONS

the table 6. Contrary to the time averaged comparison, the calculated spatially averaged fuel regression is in very good agreement with the experimental instantaneous fuel regression rate for each instant. The highest discrepancy, -5.1 %, is observed at $t = 7.5$ s. A reproduction of spatially averaged fuel regression rate is therefore realised as the instantaneous fuel regression rate uncertainty is located between 7 and 8 %.

Table 6: Comparison between the experimental instantaneous space averaged fuel regression rate and calculated space averaged fuel regression from each instant case

case	t = 5.5 s	t = 7.5 s	t = 9.5 s
D_{port} (mm)	25.9	27.4	28.9
$v_{reg,m}^{exp}$ (mm.s ⁻¹)	0.38	0.39	0.35
$v_{reg,m}^{num}$ (mm.s ⁻¹)	0.39	0.37	0.36
$\epsilon(v_{reg,m})$ (%)	2.6	-5.1	2.9

The numerical modelling is therefore validated temporally in short firing test. However, the oxidizer-to-fuel ratio shift phenomenon cannot be noticed as no particular monotonous trend is observed, corroborated by the linear diameter evolution with time. The main reason is a too short burning time and, consequently, the presented comparison cannot be comprehensive to validate temporally the numerical modelling. Longer firing test is therefore required to seize comprehensively the temporal limits of the presented validation process.

5. Conclusions and perspectives

A numerical modelling of the intern ballistic of hybrid rocket engine with the GSI model has been developed to be able to represent the aero-thermal phenomena in the combustion chamber to get complementary information to experimental data. To be effective, the presented modelling requires therefore spatial and temporal validations of the fuel regression rate as the fuel mass flow rate is a key parameter on the combustion process and, consequently, on performances. Firstly, the time averaged fuel regression rate profiles along the port are compared between the experimental data and numerical results. The time averaged fuel regression rate profile comparisons have shown that the constant diameter hypothesis for the final instant computation is not valid for the reproduction of spatial fuel regression rate distribution along the fuel port, even though the spatial-time fuel regression rate discrepancy is lower than 10 %. Considering a more realistic shape for the final diameter profile along the port is required. However, the first order approximation have shown very unstable results even though the trends seem improved. Higher interpolation order or more measurements are needed to validate the modelling. Secondly, temporal validation of spatially averaged fuel regression is also performed by comparing the results obtained by a ballistic reconstruction technique and a series of numerical computations of which each corresponds to a chosen instant. The comparisons have shown very good agreements between numerical simulations and experimental data. However, the ballistic reconstruction technique turns out to be very sensitive to the burning time uncertainty which requires a better estimation than proposed in this study. Furthermore, the time evolution of fuel regression rate does not display clues about the oxidizer-to-fuel ratio shift because the burning time of the HYCAT 12 firing test is too short and the fuel regression is very small. Hence, the temporal validation is not comprehensive enough to show the ability of numerical modelling to simulate instant related to the oxidizer-to-fuel ratio deviation.

To improve the validation method, a firing test with a longer hybrid phase is required. Currently, the HYCAT 23, with a burning time equal to 17.3 s is in analysis to support the validation of numerical modelling. Further studies will be carried out to extend the modelling to swirl injection configuration. Besides, the ballistic reconstruction technique will be superseded by the Ultrasonic pulse-echo technique to catch locally the instantaneous fuel regression rate.

6. Acknowledgements

This research is supported by ONERA and Région Occitanie, award no. DESR-SRI/15066464. We thank specially Dmitry Davidenko from ONERA for his helpfully expertise on energy modelling in the CEDRE software.

References

- [1] P.S. Andersen, W.M. Kays, and R.J. Moffat. The turbulent boundary layer on a porous plate: An experimental study of the fluid mechanics for adverse free-stream pressure gradients. Technical Report 19720022609, NASA-CR-127817, HMT-15, May 1972.
- [2] J. Anthoine, J.-Y. Lestrade, and S. Messineo, J. and Casu. Performances of a multi-pulsed hybrid rocket engine operating with highly concentrated hydrogen peroxide. In *53rd AIAA/SAE/ASEE Joint Propulsion Conference*, Atlanta, GA, jul 2017. Paper AIAA 2017-4906.
- [3] N. Bellomo, M. Lazzarin, F. Barato, and M. Grosse. Numerical investigation of the effect of a diaphragm on the performance of a hybrid rocket motor. In *46th AIAA/ASME/SAE/ASEE Joint Propulsion Conference & Exhibit*, 2010.
- [4] D. Bianchi, Nasuti F., and Delfini D. Modeling of gas-surface interface for paraffin-based hybrid rocket fuels in cfd. In *6th European Conference for Aerospace Science*, 2015.
- [5] D. Bianchi, P. Lapenna, F. Creta, and F. Nasuti. Numerical simulations of flowfield and combustion in hybrid rockets. In *Space Propulsion Conference*, 2016.
- [6] D. Bianchi, G. Leccese, F. Nasuti, and Carmicino C. Modeling of high density polyethylene regression rate in the simulation of hybrid rocket flowfields. In *7th European Conference for Aerospace Sciences*, number 629, Milan, Italy, 2017.
- [7] A. Bonfiglioli and R. Paciorri. Convergence analysis of shock-capturing and shock-fitting solutions on unstructured grids. *AIAA Journal*, 52(7):1404–1416, January 2014.
- [8] C. Carmicino and A. Russo Sorge. Role of injection in hybrid rockets regression rate behavior. *Journal of Propulsion and Power*, 21(4):606–612, July-August 2005.
- [9] C. Carmicino and A. Russo Sorge. Influence of a conical axial injector on hybrid rocket performance. *Journal of Propulsion and Power*, 22(5):984–995, 2006.
- [10] C. Carmicino and A.R. Sorge. Performance comparison between two different injector configurations in a hybrid rocket. *Aerospace Science and Technology*, 11(1):61 – 67, 2007.
- [11] G. Cheng, R. Farmer, H. Jones, and J. McFarlane. Numerical simulation of the internal ballistics of a hybrid rocket motor. In *32nd Aerospace Sciences Meeting and Exhibit*, Reno, NV, 1994. AIAA Paper 1994-554.
- [12] M.J. Chiaverini, N. Serin, D.K. Johnson, Y.-C. Lu, K.K. Kuo, and G.A. Risha. Regression rate behavior of hybrid rocket solid fuels. *Journal of Propulsion and Power*, 16(1):125–132, jan 2000.
- [13] A. Coronetti and W.A. Sirignano. Numerical analysis of hybrid rocket combustion. *Journal of Propulsion and Power*, 29:371–384, March 2013.
- [14] G. Di Martino, S. Mungiguerra, C. Carmicino, and R. Savino. Combined fluid-dynamic modelling of hybrid rocket internal ballistics and nozzle heat transfer. In *7th European Conference for Aerospace Sciences*, 07 2017.
- [15] J.-É. Durand, F. Raynaud, J. M. Lamet, L. Tessé, J.-Y. Lestrade, and J. Anthoine. Numerical study of fuel regression in hybrid rocket engine. In *2018 Joint Propulsion Conference, AIAA Propulsion and Energy Forum*, Cincinnati, OH, 2018. AIAA Paper 2018-4593.
- [16] E. Farbar, J. Louwers, and T. Kaya. Investigation of metallized and nonmetallized hydroxyl terminated polybutadiene/hydrogen peroxide hybrid rockets. *Journal of Propulsion and Power*, 23(2):476–486, 2007.
- [17] G. Gariani, F. Maggi, and L. Galfetti. Numerical simulation of HTPB combustion in a 2D hybrid slab combustor. *Acta Astronautica*, 69(5-6):289–296, sep 2011.
- [18] P. George, S. Krishnan, P. M. Varkey, M. Ravindran, and L. Ramachandran. Fuel regression rate in hydroxyl-terminated-polybutadiene/gaseous-oxygen hybrid rocket motors. *Journal of Propulsion and Power*, 17(1):35–42, 2001.
- [19] R. Hink. Validation of the k-omega turbulence model for the thermal boundary layer profile of effusive cooled walls. *CEAS Space Journal*, 7(3):389–398, sept. 2015.

- [20] R. Kumar and P.A. Ramakrishna. Measurement of regression rate in hybrid rocket using combustion chamber pressure. *Acta Astronautica*, 103:226–234, 2014.
- [21] G. Leccese, D. Bianchi, and F. Nasuti. Modeling of paraffin-based fuels in the simulation of hybrid rocket flowfields. In *52nd AIAA/SAE/ASEE Joint Propulsion Conference*. American Institute of Aeronautics and Astronautics, 2016.
- [22] G. Leccese, D. Bianchi, and F. Nasuti. Simulations of hybrid rocket flowfields including modeling of fuel pyrolysis and thermal radiation. In *Space Propulsion Conference*, 2016.
- [23] G. Lengellé, B. Fourest, Godon J.C., and C. Guin. Condensed phase behavior and ablation rate of fuels for hybrid propulsion. In *AIAA/SAE/ASME/ASEE 29th Joint Propulsion Conference and Exhibit*, Monterey, CA, 1993. AIAA Paper 1993–2413.
- [24] J.-Y. Lestrade, J. Anthoine, O. Verberne, A. J. Boiron, G. Khimeche, and C. Figus. Experimental demonstration of the vacuum specific impulse of a hybrid rocket engine. *Journal of Spacecraft and Rockets*, 54(1):101–108, jan 2017.
- [25] J.-Y. Lestrade, P. Prévot, J. Messineo, J. Anthoine, S. Casu, and B. Geiger. Development of a catalyst for high concentrated hydrogen peroxide. In *6th International Symposium on Propulsion for Space Transportation (Space Propulsion)*. SP2016–3125136, 2016.
- [26] J.L. Lin. Two-phase flow effect on hybrid rocket combustion. *Acta Astronautica*, 65(7):1042–1057, 2009.
- [27] G. Marxman and M. Gilbert. Turbulent boundary layer combustion in the hybrid rocket. *Symposium (International) on Combustion*, 9(1):371–383, jan 1963.
- [28] F. R. Menter. Two-equation eddy-viscosity turbulence models for engineering applications. *AIAA Journal*, 32(8):1598–1605, aug 1994.
- [29] R. Moffat and W. Kays. The turbulent boundary layer on a porous plate: Experimental heat transfer with uniform blowing and suction. *International Journal of Heat and Mass Transfer*, 11(10):1547 – 1566, 1968.
- [30] A. Refloch, B. Courbet, A. Murrone, P. Villedieu, C. Laurent, P. Gilbank, J. Troyes, L. Tessier, G. Chaineray, and J.B. Dargaud. Cedre software. *The ONERA Journal AerospaceLab*, pages 3–5, March 2011.
- [31] A. Russo Sorge and C. Carmicino. Non-intrusive regression rate measurements in a hybrid rocket. *RTO AVT*, (33):1–14, Sept. 2002. RTO-MP-091.
- [32] A. Russo Sorge, A. Esposito, G. Quaranta, and G. Torella. Regression rate measurements in a hybrid rocket. In *36th AIAA/ASME/SAE/ASEE Joint Propulsion Conference and Exhibit*, Las Vegas, NV, 2000. AIAA Paper 2000–3438.
- [33] V. Sankaran. Computational fluid dynamics modeling of hybrid rocket flowfields. In *Fundamentals of Hybrid Rocket Combustion and Propulsion*, volume 218, chapter 8, page 334. Progress in Astronautics and Aeronautics, edited by Chiaverini, M. J. and Kuo, K. K., 2007.
- [34] F. Shan, L. Hou, and Y. Piao. Combustion performance and scale effect from n₂o/htpb hybrid rocket motor simulations. *Acta Astronautica*, 85:1–11, 04 2013.
- [35] H. Tian, XinTian Li, NanJia Yu, and G. Cai. Numerical and experimental investigation on the effects of aft mixing chamber diaphragm in hybrid rocket motor. 56(11):2721, 2013.
- [36] E.F. Toro, M. Spruce, and W. Speares. Restoration of the contact surface in the hll-riemann solver. *Shock Waves*, 4(1):25–34, July 1994.
- [37] E. J. Wernimont and S. D. Heister. Reconstruction technique for reducing hybrid-rocket combustion test data. *Journal of Propulsion and Power*, 15(1):128–136, jan 1999.
- [38] C. K. Westbrook and F. L. Dryer. Simplified reaction mechanisms for the oxidation of hydrocarbon fuels in flames. *Combustion Science and Technology*, 27(1-2):31–43, dec 1981.
- [39] D. C. Wilcox. Reassessment of the scale-determining equation for advanced turbulence models. *AIAA Journal*, 26(11):1299–1310, nov 1988.

FUEL REGRESSION MODELLING FOR HYBRID ROCKET CFD SIMULATIONS

- [40] D.C. Wilcox. Effects of compressibility. In *Turbulence Modeling For CFD*, volume 1, chapter 5, pages 243–251. DCW Industries, 3rd edition, 2006.
- [41] D.C. Wilcox. One–equation and two–equation models. In *Turbulence Modeling For CFD*, volume 1, chapter 4, pages 192–209. DCW Industries, 3rd edition, 2006.
- [42] S. Zhang, F. Hu, D. Wang, P. Okolo, and W. Zhang. Numerical simulations on unsteady operation processes of n2o/htpb hybrid rocket motor with/without diaphragm. *Acta Astronautica*, 136:115 –124, 2017.